

Design and Characteristics of an X-ray Laser Oscillator

A. Halavanau,¹ A. Benediktovitch,² A.A. Lutman,¹ D. DePonte,¹
D. Cocco,³ N. Rorhinger,^{2,4} U. Bergmann,¹ and C. Pellegrini¹

¹SLAC National Accelerator Laboratory, Menlo Park, CA 94025, USA

²Center for Free Electron Laser Science, DESY, Hamburg 22607, Germany

³Lawrence Berkeley National Laboratory, Berkeley, CA 94720, USA

⁴Department of Physics, Universität Hamburg, Hamburg 22761, Germany

Amplified spontaneous emission (ASE) of the $K\alpha_1$ line and seeded amplified emission of the $K\beta$ lines have been recently observed for Ne gas, Cu compounds and Mn solutions at the LCLS and SACLA X-ray free electron lasers (XFELs), using an X-ray SASE pulse as a pump to create population inversion. In this Letter, we propose to use a train of SASE pump pulses, e.g. from LCLS, impinging on a liquid jet of cupric nitrate in a tunable crystal Bragg cavity, to realize an X-ray laser oscillator (XLO) at the Cu $K\alpha_1$ line. XLO is a novel X-ray source generating fully coherent, transform limited 8 keV X-ray pulses with high photon numbers ($> 5 \times 10^{10}$ ph/pulse) and high spectral resolution (48 meV), tunable over a ~ 3 eV range. Using different elements, e.g. Mn, Fe, Zn, etc., XLOs with discrete photon energies in the range of 5 to 12 keV are feasible. With its unique characteristics XLOs will extend research in atomic and molecular science beyond current capabilities.

PACS numbers: 41.60.Cr, 41.50.+h, 42.55.Vc

With their unique properties of high peak power, femtosecond (fs) pulse duration, and transverse coherence, X-ray Free Electron Lasers (XFELs) have proven to be a revolutionary new tool in the nanometer to angstrom wavelength region, with a wide range of scientific applications [1, 2]. However most XFELs operate in self-amplified spontaneous emission (SASE) mode [3, 4], where the X-ray pulse is started from electron shot-noise. Due to the stochastic nature of this process, the resulting X-ray pulses have limited longitudinal coherence, yielding significant shot-to-shot spectral, temporal, and intensity fluctuations.

In the VUV and XUV regions, various seeding schemes including High Gain Harmonic Generation (HG) [5–7] and Echo Enabled Harmonic Generation (EEHG) [8, 9] have been successfully employed to improve the longitudinal coherence and reduce intensity fluctuations. At shorter wavelengths, self-seeding schemes based on gratings (soft x-rays) and transmissive or reflective Bragg monochromators (hard X-rays) have been successfully employed to increase the longitudinal coherence and the spectral brightness [10–16]. The bandwidth of self-seeded soft X-ray pulses, e.g. at LCLS, is reduced by one order of magnitude with respect to SASE pulses, typically from about 10^{-3} to 10^{-4} , but the pulses are not transform limited and may require further monochromatization to reduce unwanted background from spectral pedestals [17, 18]. Self-seeding schemes also suffer from large intensity fluctuations, caused by the variations of the seed power after the intra-undulator monochromator and by fluctuations in energy and intensity of the electron beam [19].

To produce transform limited FEL pulses, one can reduce the pulse duration down to a single coherent spike,

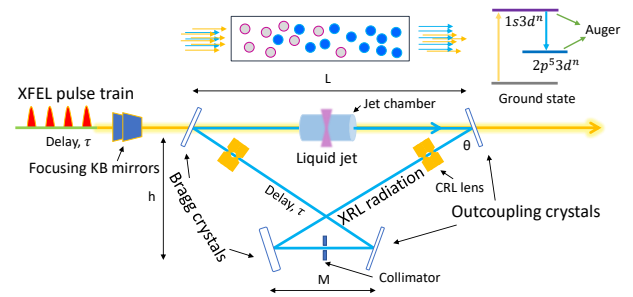


FIG. 1. XLO schematics. A train of SASE pulses with spacing τ impinges on a liquid jet, generating population inversion and photon emission. The amplified $K\alpha_1$ signal is recirculated with a roundtrip time that matches τ and outcoupled after N passes. In the figure, the separation between X-ray pump pulses and the cavity size is not to scale.

by making the electron bunch length shorter than the cooperation length [20]. The use of emittance spoilers [21–23], the combination of fresh-slice, cascaded amplification [24, 25], non-linear compression schemes [26] and recently eSASE [27] have succeeded in producing such pulses. However, in these schemes the coherence is achieved by decreasing the pulse duration, resulting in a larger bandwidth and lower photon flux compared to self-seeded modes as well as large shot-to-shot fluctuations.

As in the optical regime, ideally one would like to have an intense, transform limited, fully coherent, shot-to-shot stable, single mode pulse. A number of schemes have been proposed, but not yet demonstrated, to produce such pulses, including the double bunch FEL (DBFEL), the regenerative amplifier (RAFEL) and the X-ray FEL

oscillator (XFEL) [28–31]. While DBFEL might reach very high power levels (approaching TW) and near transform limited pulses, it still suffers from shot-to-shot power fluctuations. The technical challenges for RAFEL and XFEL are mechanical stability, radiation focusing, temporal and transverse beam overlap in the large diamond Bragg crystal cavity wrapped around a long undulator section (40 and 130 m). Ultimately, XFEL could operate with a high-repetition rate temporally equispaced set of long bunches, achieving ultra-narrow bandwidth, about 10^{-6} .

In this Letter, we propose a novel approach for producing stable, high power, narrow-band hard X-ray pulses based on employing a population inversion gain medium within an oscillator cavity that is periodically pumped by a train of SASE pulses from an XFEL, as schematically shown in Fig. 1. Amplified Spontaneous Emission (ASE) has been observed and studied for Ne gas [32], Cu metal foils [33] and recently for Mn solutions [34]. Here, an intense pump pulse creates a 1s core-hole and spontaneously emitted $K\alpha$ fluorescence photons along the direction of the population inversion are amplified. Depending on the pump intensity and gain medium, very high values of gain (up to 2×10^6) were observed and $K\alpha_1$ ASE pulses of up to 8×10^7 photons/pulse were created starting from noise [34].

The XLO system described here and shown in Fig. 1 starts with a SASE pump pulse that creates a 1s corehole population inversion followed by ASE in a liquid jet of a concentrated cupric nitrate ($\text{Cu}(\text{NO}_3)_2$) solution, with about 4.2 Cu atoms per nm^3 . After the initial ASE gain in the first pass, the $K\alpha_1$ signal is recirculated through the cavity and matched with the arrival of the subsequent XFEL pulse from the pulse train, creating seeded stimulated emission. Once saturation is achieved after 4-8 round trips, the pulse will be outcoupled from the cavity. We have chosen a cupric nitrate solution as a gain medium because the copper $K\alpha_1$ photon energy at 8 keV is widely used in X-ray science. Furthermore, cupric nitrate is soluble in high concentrations, does not contain any heavy elements that would reduce the gain by absorbing 8 keV photons, and is straightforward to handle. While we focus on the Cu $K\alpha_1$ line and a Si (444) crystal Bragg cavity geometry that matches its wavelength, the XLO concept is not limited to Cu $K\alpha_1$ line, and other choices of the lasing medium and matching cavity configurations are possible. In fact, it is possible to switch between different lasing media with minimal change in the cavity geometry. For example, the Fe $K\alpha_1$ line at 6.4 keV using a Si (333) Bragg reflection with 67.9 degree Bragg angle, can be easily realigned to match the Zn $K\alpha_1$ line at 8.6 keV switching to the Si (444) reflection with a slight realignment to a 66.3 degree Bragg angle.

The XLO Bragg cavity length C_l can range from approximately 50 cm to a few meters, depending on the value of SASE train separation τ from 1.7 - 10 ns. The

cavity length C_l and lateral size h are related to the upper and lower crystals separation L , M and Bragg angle θ by: $(L + M) = C_l / (1 - 1 / \cos 2\theta)$ and $h = -\frac{1}{2}(L + M) \tan 2\theta$, where $C_l = c\tau$. The optimal size is a compromise between ensuring sufficient time to replace the lasing medium between subsequent pulses in the train, and guaranteeing sufficient mechanical/temperature stability of the cavity. The resulting X-ray laser pulses are highly monochromatic (as defined by the Bragg optics in the cavity), transform limited, and provide one order of magnitude higher pulse energy with significantly enhanced stability compared to monochromatized SASE pulses. While the tunability is limited to the width of the emission line (3-5 eV), such XLOs can be built for various discrete energies using different emission lines that match the desired experimental parameters. The unprecedented pulse quality resulting from this approach will enhance the use of XFELs for a wide range of hard X-ray applications, including coherent X-ray imaging, x-ray scattering, and X-ray interferometry [35].

To effectively pump the lasing medium, we propose to use a KB mirror setup, upstream of the XLO, as previously employed in the LCLS Mn ASE experiments [34]. Such a setup exists at the LCLS Coherent X-ray Imaging (CXI) instrument, and similar systems are available at the SACLA BL3 and Eu-XFEL SFX beamlines. For the wavelength considered in this study, Silicon and Diamond are optimal for the cavity optics. The characteristics of these two crystals for various diffraction planes, matching the Cu $K\alpha_1$ emission line are reported in Tab. I and calculated with dynamical diffraction code XOP [36]. The ASE beam divergence depends on the aspect ratio of beam size and gain length and is of order 1 mrad, well above the Si crystal angular acceptance for good reflectivity. Hence, on the first pass the cavity losses are large, and need to be overcompensated by a large XLO laser gain (10^4). At the following passes the losses will be much smaller since the angular spread of the amplified photons matches the crystal acceptance.

To analyze the XLO performance we first consider the amplification process in the lasing medium. The emission from the population-inverted medium is calculated using a correlation function approach [38, 39]. We use the XATOM software [40, 41] to evaluate the photoionization cross section of the copper atom 1s level and the Auger decay time to be 0.0324 Mb and 823 as. The evolution of atomic populations is computed, in a 1D model approximation, via a two-point correlation function of the atomic coherences (polarization) and two-time correlation function of fields.

At the initial stage of the emission, the spontaneously emitted radiation (described in terms of field correlation function) triggers the amplification process. During the propagation through the population inverted medium, the radiation is amplified and the contribution of the spontaneous emission becomes negligible compared to

amplified stimulated emission. At this point, the field correlation function can be factorized into classical field amplitudes. Corresponding equations (after neglecting the spontaneous emission contributions) can be factorized as well and become equivalent to the Maxwell-Bloch equations. The field obtained is propagated through the Bragg crystal cavity elements and is used as a seed for the next round of amplification. Starting with the second round, the spontaneous $K\alpha_1$ emission along the gain medium is much weaker than the recirculated seeding field and the contribution of the spontaneous emission terms can be neglected leading to a description in terms of Maxwell-Bloch equations. In a similar way, Maxwell-Bloch equations are used for the subsequent rounds of amplification.

Photons are recirculated using a tunable four bounce bowtie (+ - - +) Bragg crystal cavity [44], as shown in Fig. 1. Its optical properties are graphed in Fig. 2. The bowtie cavity is tuned to ensure the exact spectral alignment of the Cu $K\alpha_1$ peak wavelength with the Bragg reflection angle and temporal alignment with the pulse train separation τ . The first crystal (upper left) is thin and highly transparent for the incident pump pulse at 9 keV, yet highly reflective at the Bragg angle of the Cu $K\alpha_1$ peak. One of the other three crystals (e.g. upper right in Fig. 1) is also thin but highly reflective at the chosen wavelength. It is used to outcouple the X-ray pulse when it has reached saturation after several amplification cycles. Outcoupling is done by switching to a status with large transmission and near zero reflection. Several techniques for radiation outcoupling, e.g. a small fast rotation or heating with a laser pulse, can be employed and are currently being studied [45, 46]. We choose the backscattering Bragg geometry as it provides a large angular acceptance while reducing the bandwidth, see Tab.I and Fig. 2. The Darwin width of the Bragg reflection defines the spectral-angular acceptance and the corresponding X-ray pulse length and lasing medium radius. Using the Si (444) reflection gives a 48 meV bandwidth, while the diamond $C^*(400)$ reflection gives a 65 meV bandwidth with a more than two times smaller angular acceptance. The cavity tolerances in the crystal angle and position have been estimated to be of the order of $1 \mu\text{m}$ and $1 \mu\text{rad}$, well within the capability of present day crystal support and alignment systems.

To understand the salient features of the XLO cavity we use the formalism of Fourier optics and dynamic diffraction theory in perfect crystals [47–50]. We select flat symmetric crystals to alleviate any additional azimuthal angle effects on the Bragg diffraction [47]. We evaluate the crystals Darwin reflectivity curves, thickness and Miller indices using the XOP code [36]. The curves obtained are then convoluted with the spectral content of the electromagnetic field. The correction to the Bragg angle θ_B for a Gaussian photon beam is given by a simple geometric relation $\sin \theta_B \approx \sin \theta_{B_0}(1 - \Delta\phi^2/2)$, where

(hkl)	θ_B (deg)	$\Delta\theta$ (μrad)	$\Delta\omega$ (meV)	$\Delta\omega/\omega \cdot 10^{-6}$	τ (fs)
Silicon					
333	47.5	10.3	76.0	9.4	23.7
533	68.5	12.5	39.6	5.0	45.5
444	79.3	31.6	48.1	6.0	37.4
Diamond					
311	45.7	9.6	75.4	9.4	23.9
400	59.8	14.0	65.6	8.1	27.4
331	70.3	13.0	37.4	4.7	48.1

TABLE I. Silicon and Diamond crystal parameters for 8048 eV photons in different Bragg reflection geometries.

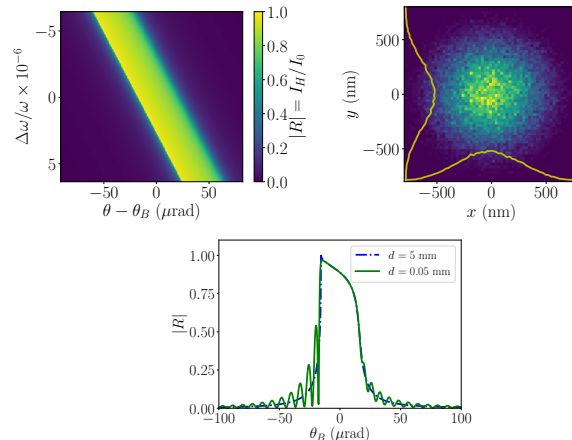


FIG. 2. DuMond diagram of Si (444) crystal at 8048 eV (top left). Refocused ASE radiation at the jet location after two sets of Be lenses with state of the art shape profiles (top right). Darwin curve for Bragg reflection of 8048 eV photons, corrected for refraction for the cases of thick ($d = 5 \text{ mm}$) and thin ($d = 50 \mu\text{m}$) flat Si (444) crystals at room temperature (bottom).

θ_{B_0} is the Bragg angle for a non-divergent beam and ϕ is the vertical angle with respect to the plane perpendicular to the crystal surface. The effect of vertical divergence is of a second order for $|\Delta\phi| < 10^{-3}$ rad and will leave the radiation field mostly intact in ϕ , while selecting in θ .

The cavity losses are defined by the crystal angular and energy acceptance. The ASE signal angular divergence is approximately defined by the geometry of the lasing medium (1 mrad vertical, 2 mrad horizontal), leading to 99.7% cavity losses for the first pass. The crystal reflectivity curve $|R|$ presented in Fig. 2 (bottom), where $|R| = I_H/I_0$, for the initial radiation intensity I_0 and diffracted intensity I_H . Furthermore, we utilize a set of two compound refractive lens (CRL) assemblies of $f = 52 \text{ cm}$ and a collimator in a 4 m cavity to refocus the amplified signal on the jet after four reflections. Fourier optics simulation results corroborate this requirement; see Fig. 2 (top right). After the first pass, the cavity efficiency is given by the crystal reflectivity and the losses in the focusing lenses. We estimate the total efficiency in second

and later passes to be about 41%.

Note that, based on Mn ASE results [34] we can obtain up to almost $10^8 K\alpha_1$ photons in the initial pass, providing more than enough signal to overcome the first pass large cavity losses. We now present the results of numerical simulations done using the one-dimensional code [38], for cupric nitrate as a gain medium, for different values of the pumping power and number of passes in the XLO cavity. The parameters for the simulations are determined by the LCLS pump power and pulse duration, by the optical cavity properties, and by the gain medium geometry. For 9 keV LCLS SASE X-ray pulses we can assume a peak power of 30 to 50 GW with a pulse duration variable between 20 to 60 fs. Using 33.6 GW 60 fs pulse, the corresponding pulse energy is 2 mJ, well within LCLS capabilities.

The cavity crystals define a horizontal angular acceptance of $31.6 \mu\text{rad}$; see Tab. I. To alleviate the effect of diffraction, one must satisfy $d\Delta\theta \geq \lambda/4\pi$, which yields $d \geq 390 \text{ nm}$. The gain medium can be described as a thin cylinder of length $300 \mu\text{m}$, defined by the jet diameter, along the pump pulse direction of propagation and an effective radius defined by the KB focusing properties for 9 keV X-ray pump pulse. In our calculation, we assume a gain medium diameter of 800 nm , satisfying the above condition and justifying the use of a 1D simulation code. At this spot size, the Rayleigh length is $z_R = 3.65 \text{ mm}$, i.e. much longer than the jet size. The vertical angular acceptance is much larger than horizontal, and hence we could optimize the system by having an elliptically shaped pump pulse. While in principle, this solution can yield a better XLO performance, for sake of simplicity, we consider only the case of a gain medium with circular cross section, with the radius defined by the horizontal acceptance. In addition to varying the pump pulse intensity, the gain can also be controlled by the focusing KB optics, albeit with slightly larger cavity losses.

Another important quantity is the number of Cu atoms in the gain medium. Assuming $300 \mu\text{m}$ length and a 800 nm diameter, there are $6.3 \cdot 10^{11}$ Cu atoms in the lasing volume, which sets the upper limit for the number of XLO photons at saturation. We denote the initial pass as $n = 0$, and following passes as $n = \bar{1}, \bar{N}$, where $N = 7$. Depending on the pump pulse parameters, in the initial pass the ASE process generates about $10^3 - 10^4$ photons starting from noise. After 7 additional passes the total number of XLO photons in saturation reaches up to $7 \cdot 10^{10}$, as shown in Fig. 3.

We first consider high gain XLO regime: with 8 pump pulses of 2 mJ. In this case, rapid saturation occurs as early as in the third pass. The maximum number of photons for a $300 \mu\text{m}$ diameter jet is about $7 \cdot 10^{10}$. Thus, the XLO brightness is comparable with existing hard x-ray self-seeding (HXRSS) XFEL, while offering an order of magnitude reduction in bandwidth and much better stability. We then consider the low gain case with a SASE

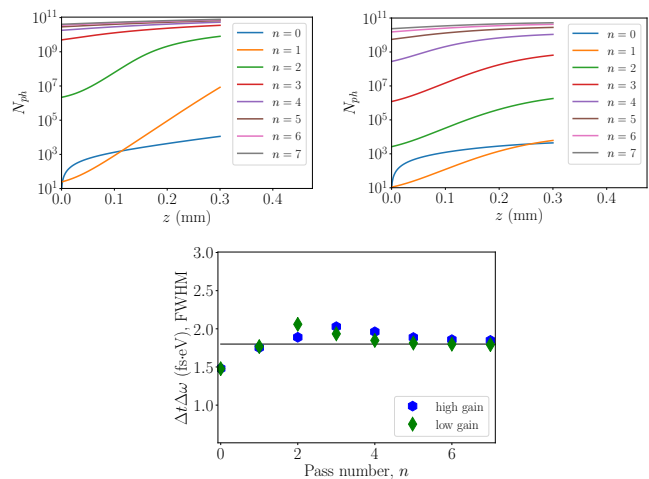


FIG. 3. XLO in high-gain (top left) and low-gain (top right) regimes and resulting time-bandwidth products (bottom). The solid black line corresponds to $\Delta t \Delta \omega = 1.8 \text{ fs-eV}$.

train of 8 pulses of 1 mJ, thus reducing the gain in the medium, and gradually building up the cavity power.

In this case, radiation supermodes start to form, similarly to [52, 53]. We note that the mode shape is determined by the nonlinear gain, pictured in Fig. 3 and crystal reflectivity shown in Fig. 2. After 4 passes, the resulting XLO radiation time-bandwidth product is essentially transform-limited and is equal to 1.8 fs-eV .

Multi-bunch LCLS Cu linac capability has been demonstrated previously with up to 4 bunches and various time separations from 10 to 200 ns [54–56]. In the low-gain regime, we expect to raise the number of linac pulses to 8. The SASE pump creates a plasma channel of high temperature, giving rise to a shock wave (rarefaction wave) and the lasing medium must be replenished before the next pump pulse arrives, and the stability of the jet has to be guaranteed. Recent experiments with slow water jets ($\leq 30 \text{ m/s}$) and LCLS Cu linac two-bunch mode [57] revealed the shock wave travel time to be of the order of tens of nanoseconds. We are now testing similar effects with more powerful jets that have much higher speeds. The minimal replenishing time T_{medium} will ultimately define the smallest realistic cavity size for XLO operation [58, 59]. Furthermore, the cavity transit time, T_{CAV} , must also be a multiple of the linac RF period $T_{RF}=350 \text{ ps}$: $\tau = T_{CAV} = nT_{RF} > T_{medium}$. The advantages when using a small τ are reduced time jitter in the SASE pump pulses, and more stability due to a compact cavity size.

In conclusion, we present a novel scheme to realize an XLO operating in the 5 to 12 keV photon energy range using an XFEL pulse train as a periodic pump and a liquid jet gain medium. We discuss the oscillator's cavity, based on Bragg reflection optics in a bowtie configuration and explore the performance of a cupric nitrate lasing

medium in various gain regimes. We show that the XLO can generate intense X-ray pulses that are transversely coherent and nearly or fully transform limited, with a FWHM bandwidth of 48 meV. The potential scientific applications of this novel X-ray source are extensive and include coherent imaging, inelastic scattering, X-ray interferometry.

ACKNOWLEDGEMENTS

This work was supported by the U.S. Department of Energy Contract No. DE-AC02-76SF00515. Authors would like to thank G. Marcus, A. Marinelli, Y. Shvyd'ko and Z. Huang for the valuable suggestions throughout the research.

-
- [1] C. Bostedt, *et al*, **Linac coherent light source: The first five years**. *Rev. Mod. Phys.*, 88:015007, Mar 2016.
- [2] U. Bergmann, V. Yachandra, and J. Yano, editors. **X-Ray Free Electron Lasers**. Energy and Environment Series. The Royal Society of Chemistry, 2017.
- [3] R. Bonifacio, C. Pellegrini, and L. Narducci. **Collective Instabilities and High Gain Regime in a Free Electron Laser**. *Opt. Commun.*, 50:373–378, 1984.
- [4] Ya.S. Derbenev, A.M. Kondratenko, and E.L. Saldin. **On the possibility of using a free electron laser for polarization of electrons in storage rings**. *Nuclear Instruments and Methods in Physics Research*, 193(3):415 – 421, 1982.
- [5] L. H. Yu. **Generation of intense UV radiation by subharmonically seeded single-pass free-electron lasers**. *Phys. Rev. A*, 44:5178–5193, Oct 1991.
- [6] E. Allaria, *et al*, **Highly coherent and stable pulses from the fermi seeded free-electron laser in the extreme ultraviolet**. *Nature Photonics*, 6:699–704, 09 2012.
- [7] E. Allaria, *et al*, **Two-stage seeded soft-x-ray free-electron laser**. *Nature Photonics*, 7:913–918, 10 2013.
- [8] G. Stupakov. **Using the beam-echo effect for generation of short-wavelength radiation**. *Phys. Rev. Lett.*, 102 7:074801, 2009.
- [9] P. Ribic, *et al*, **Coherent soft x-ray pulses from an echo-enabled harmonic generation free-electron laser**. *Nature Photonics*, 13:1–7, 08 2019.
- [10] D. Ratner, *et al*, **Experimental demonstration of a soft x-ray self-seeded free-electron laser**. *Phys. Rev. Lett.*, 114:054801, Feb 2015.
- [11] T. Kroll, *et al*, **X-ray absorption spectroscopy using a self-seeded soft x-ray free-electron laser**. *Opt. Express*, 24(20):22469–22480, Oct 2016.
- [12] G. Geloni, V. Kocharyan, and E. Saldin. **A novel self-seeding scheme for hard x-ray fels**. *Journal of Modern Optics*, 58(16):1391–1403, 2011.
- [13] J. Amann, *et al*, **Demonstration of self-seeding in a hard-X-ray free-electron laser**. *Nature Photonics*, 6:693–698, Oct 2012.
- [14] A. A. Lutman, *et al*, **Demonstration of single-crystal self-seeded two-color x-ray free-electron lasers**. *Phys. Rev. Lett.*, 113:254801, Dec 2014.
- [15] T. Osaka, *et al*, **A micro channel-cut crystal X-ray monochromator for a self-seeded hard X-ray free-electron laser**. *Journal of Synchrotron Radiation*, 26(5):1496–1502, Sep 2019.
- [16] I. Inoue, *et al*, **Generation of narrow-band x-ray free-electron laser via reflection self-seeding**. *Nature Photonics*, 13:1, 05 2019.
- [17] G. Marcus, *et al*, **Experimental observations of seed growth and accompanying pedestal contamination in a self-seeded, soft x-ray free-electron laser**. *Phys. Rev. Accel. Beams*, 22:080702, Aug 2019.
- [18] E. Hemsing, A. Halavanau, Z. Zhang, **Statistical theory of a self-seeded free electron laser with noise pedestal growth**. *Phys. Rev. AB*, 2019. Accepted in PRAB.
- [19] W. Colocho, *et al*, **Increased stability requirements for seeded beams at LCLS**. In Proc. of FEL13, New York City, NY, USA 2013.
- [20] S. Reiche, P. Musumeci, C. Pellegrini, J.B. Rosenzweig **Development of ultra-short pulse, single coherent spike for SASE X-ray FELs** *NIM:A*, 593, 1, pp. 45-48, (2008).
- [21] P. Emma, K. Bane, M. Cornacchia, Z. Huang, H. Schlarb, G. Stupakov, and D. Walz. **Femtosecond and subfemtosecond x-ray pulses from a self-amplified spontaneous-emission-based free-electron laser**. *Phys. Rev. Lett.*, 92:074801, Feb 2004.
- [22] Y. Ding, *et al*, **Generating femtosecond x-ray pulses using an emittance-spoiling foil in free-electron lasers**. *Applied Physics Letters*, 107(19):191104, 2015.
- [23] A. Marinelli, J. MacArthur, P. Emma, M. Guetg, C. Field, D. Kharakh, A. A. Lutman, Y. Ding, and Z. Huang. **Experimental demonstration of a single-spike hard-x-ray free-electron laser starting from noise**. *Applied Physics Letters*, 111(15):151101, 2017.
- [24] A. A. Lutman, *et al*, **Fresh-slice multicolour x-ray free-electron lasers**. *Nature Photonics*, 10:745 EP –, Oct 2016. Article.
- [25] A. A. Lutman, *et al*, **High-Power Femtosecond Soft X Rays from Fresh-Slice Multistage Free-Electron Lasers**. *Phys. Rev. Lett.*, 120(26):264801, 2018.
- [26] S. Huang, *et al*, **Generating single-spike hard x-ray pulses with nonlinear bunch compression in free-electron lasers**. *Phys. Rev. Lett.*, 119:154801, Oct 2017.
- [27] J. Duris, *et al*, **Tunable isolated attosecond X-ray pulses with gigawatt peak power from a free-electron laser**. *Nature Photonics*, 1749-4893, 2019.
- [28] A. Halavanau, F.-J. Decker, C. Emma, J. Sheppard, and C. Pellegrini. **Very high brightness and power LCLS-II hard X-ray pulses**. *Journal of Synchrotron Radiation*, 26(3), May 2019.
- [29] K.-J. Kim, Y. Shvyd'ko, and S. Reiche. **A proposal for an x-ray free-electron laser oscillator with an energy-recovery linac**. *Phys. Rev. Lett.*, 100:244802, Jun 2008.
- [30] R. Colella and A. Luccio. **Proposal for a free electron laser in the x-ray region**. *Optics Communications*, 50(1):41 – 44, 1984.
- [31] Z. Huang and R. D. Ruth. **Fully coherent x-ray pulses from a regenerative-amplifier free-electron laser**. *Phys. Rev. Lett.*, 96:144801, Apr 2006.
- [32] N. Rohringer, *et al* **Atomic inner-shell x-ray laser at 1.46 nanometres pumped by an x-ray free-electron laser**. *Nature*, 481:488 EP –, Jan 2012.
- [33] H. Yoneda, *et al*, **Atomic inner-shell laser at 1.5-Angström wavelength pumped by an x-ray free-electron laser**. *Nature*, 524:446–449, 08 2015.

- [34] T. Kroll, *et al*, **Stimulated x-ray emission spectroscopy in transition metal complexes**. *Phys. Rev. Lett.*, 120:133203, Mar 2018.
- [35] B. Adams, *et al*, **Scientific Opportunities with an X-ray Free-Electron Laser Oscillator**. arXiv:1903.09317, 2019.
- [36] M. S. del Rio and R. J. Dejus. **Xop v2.4: recent developments of the x-ray optics software toolkit**. *Proc.SPIE*, 8141:8141 – 8141 – 5, 2011.
- [37] T. Kroll, *et al*, submitted to *PRL*.
- [38] A. Benediktovitch, V. P. Majety, and N. Rohringer. **Quantum theory of superfluorescence based on two-point correlation functions**. *Phys. Rev. A*, 99:013839, Jan 2019.
- [39] L. Mercadier, *et al*, **Evidence of extreme ultraviolet superfluorescence in Xenon**. *Phys. Rev. Lett.*, 123:023201, Jul 2019.
- [40] Z. Jurek, S.-K. Son, B.Ziaja, and R. Santra. **XMDYN and XATOM: versatile simulation tools for quantitative modeling of X-ray free-electron laser induced dynamics of matter**. *Journal of Applied Crystallography*, 49(3):1048–1056, Jun 2016.
- [41] S.-K. Son, L. Young, and R. Santra. **Impact of hollow-atom formation on coherent x-ray scattering at high intensity**. *Phys. Rev. A*, 83:033402, Mar 2011.
- [42] J. A. Bearden and A. F. Burr. **Reevaluation of x-ray atomic energy levels**. *Rev. Mod. Phys.*, 39:125–142, Jan 1967.
- [43] P. Glatzel and U. Bergmann. **High resolution 1s core hole x-ray spectroscopy in 3d transition metal complexes—electronic and structural information**. *Coordination Chemistry Reviews*, 249(1):65 – 95, 2005. Synchrotron Radiation in Inorganic and Bioinorganic Chemistry.
- [44] R. M. J. Cotterill. **A universal planar x-ray resonator**. *Applied Physics Letters*, 12(12):403–404, 1968.
- [45] T. Kolodziej, P. Vodnala, S. Terentyev, V. Blank, and Y. Shvyd’ko. **Diamond drumhead crystals for X-ray optics applications**. *Journal of Applied Crystallography*, 49(4):1240–1244, Aug 2016.
- [46] Y. Shvyd’ko. **Output coupling from x-ray free-electron laser cavities with intracavity beam splitters**. *Phys. Rev. Accel. Beams*, 22:100703, Oct 2019.
- [47] B. W. Batterman and H. Cole. **Dynamical diffraction of X-rays by perfect crystals**. *Rev. Mod. Phys.*, 36:681–717, Jul 1964.
- [48] R. R. Lindberg and Yu. V. Shvyd’ko. **Time dependence of bragg forward scattering and self-seeding of hard x-ray free-electron lasers**. *Phys. Rev. ST Accel. Beams*, 15:050706, May 2012.
- [49] Y. Shvyd’ko and R. Lindberg. **Spatiotemporal response of crystals in x-ray bragg diffraction**. *Phys. Rev. ST Accel. Beams*, 15:100702, Oct 2012.
- [50] J. J. DeMarco and R. J. Weiss. **Absolute x-ray scattering factors of silicon and germanium**. *Phys. Rev.*, 137:A1869–A1871, Mar 1965.
- [51] P. Patimisco, A. Sampaolo, F. K. Tittel, and V. Spagnolo. **Mode matching of a laser-beam to a compact high finesse bow-tie optical cavity for quartz enhanced photoacoustic gas sensing**. *Sensors and Actuators A: Physical*, 267:70 – 75, 2017.
- [52] G. Dattoli, A. Marino, A. Renieri, and F. Romanelli. **Progress in the hamiltonian picture of the free-electron laser**. *IEEE Journal of Quantum Electronics*, 17(8):1371–1387, 1981.
- [53] P. Elleaume. **Microtemporal and spectral structure of storage ring free-electron lasers**. *IEEE Journal of Quantum Electronics*, 21(7):1012–1022, July 1985.
- [54] F. J. Decker, *et al*, **A demonstration of multi-bunch operation in the LCLS**. In *Proceedings of FEL2010, Malmoe, Sweden*, page 467, 2010.
- [55] F.-J. Decker, *et al*, **Two Bunches with ns-Separation with LCLS**. In *Proceedings, 37th International Free Electron Laser Conference, Daejeon, Korea, August 23-28*, page WEP023, 2015.
- [56] F.-J. Decker, K. Bane, W. Colucho, A. A. Lutman, and J. Sheppard. **Recent Developments and Plans for Two Bunch Operation with up to 1 μ s Separation at LCLS**. In *Proceedings, 38th International Free Electron Laser Conference, FEL2017*, page TUP023, 2018.
- [57] C. A. Stan, *et al*, **Liquid explosions induced by x-ray laser pulses**. *Nature Physics*, 12:966 EP, 2016.
- [58] D. Wang, U. Weierstall, L. Pollack, Lois and J. Spence. **Double-focusing mixing jet for XFEL study of chemical kinetics**. *J. of Synchr. Rad.*, 21, 6, pp. 1364-1366, 2014.
- [59] D. A. Shapiro, *et al*, **Powder diffraction from a continuous microjet of submicrometer protein crystals**. *J. of Synchr. Rad.*, 15, 6, pp. 593-599, 2008.